OI 630.0 nm Post-Sunset Emission Enhancement as an Effect of Tidal Activity over Low-Latitudes

Sovan Saha[1], Duggirala Pallamraju[1], Sunil Kumar[1], Fazlul I Laskar[2], and Nicholas Michael Pedatella[3]

[1]Physical Research Laboratory
[2]Laboratory for Atmospheric and Space Physics, University of Colorado, Boulder, CO, USA
[3]National Center for Atmospheric Research (UCAR)

December 10, 2023

OI 630.0 nm post-sunset emission enhancement as an effect of tidal activity over low-latitudes

Sovan Saha[1], Duggirala Pallamraju[1], Sunil Kumar[1], Fazlul I. Laskar[2], and Nicholas M. Pedatella[3]

[1] Space and Atmospheric Sciences Division, Physical Research Laboratory, Ahmedabad, India

[2]Laboratory for Atmospheric and Space Physics, University of Colorado, Boulder, CO, USA

[3]High Altitude Observatory, National Center for Atmospheric Research, Boulder, CO, USA

Corresponding author: Sovan Saha (sovansaha93@gmail.com).

Key Points:

· OI 630.0 nm post-sunset emission enhancement over low-latitudes is consistent with the presence of poleward meridional winds.

· WACCM-X simulated meridional winds show a poleward wind reversal during post-sunset hours, on occasion.

· Quarter-diurnal tides seem to play significant role in reversing the meridional winds after sunset.

Abstract:

The OI 630.0 nm airglow emission variability provides salient information on the dynamical changes taking place in the upper atmosphere at around 250 km. The emission rates vary with the changes in the ambient electron densities and the neutral constituents that are associated with these emissions. On several occasions, enhancements in these emissions are observed during post-sunset hours as measured from Mt. Abu (24.6°N, 72.7°E, 19°N Mag), a low-latitude location at Indian longitudes. These enhancements occur following the typical monotonic decrease in emission intensity after sunset. The presence of poleward meridional wind was shown to be the cause for such observed emission enhancements. However, climatologically, meridional winds are equatorward during these times. In this study, the cause of such reversal in winds in the post-sunset hours has been investigated using the variation in electron densities and winds simulated by the Whole Atmosphere Community Climate Model with thermosphere-ionosphere eXtension (WACCM-X), which also shows enhancements in electron densities similar to those observed in the post-sunset OI 630.0 nm nightglow emissions, and simultaneous reversal in winds as well. The amplitudes and phases of different components of tides obtained from WACCM-X meridional winds reveal a significant contribution of quarter-diurnal tides to the observed reversal in the meridional winds during post-sunset hours. The change in the tidal amplitudes is proportional to the changes in wind magnitude during that wind reversal.

1. Introduction:

The OI 630.0 nm (redline) nightglow emissions typically decrease monotonically after sunset along with the decrease in the incidence of solar radiation. The nightglow emission intensities continue to be small throughout the night and again start increasing towards morning twilight time. In one of our recent studies, an enhancement in OI 630.0 nm nightglow emissions after sunset was reported (Saha et al., 2021) in measurements over Mt. Abu (24.6°N, 72.7°E, 19°N Mag), a low-latitude location in the Indian longitude sector. The enhancements in nightglow emissions were observed between 20-22 hrs local time. Firstly, the strength of pre-reversal enhancement in the zonal electric field was investigated as a possible cause as it has the potential to bring in equatorial and off-equatorial plasma to the tropical latitudes, such as Mt. Abu. However, it could not satisfactorily explain the observations of enhancement in redline emissions during post-sunset time. The variation in meridional winds, however, showed that they were either poleward or that there was a cessation in the equatorward direction during those times. This observation was explained in terms of the altitudinal movement of the ionosphere to be responsible for the observed enhancements in the redline airglow. As the poleward wind contributes to a decrease in the ionospheric height (Saha et al., 2021), thereby, it provides greater reactants for the dissociative recombination mechanism to cause an enhancement in the emissions. Such a decrease in the height of the ionosphere in the nighttime has been observed during midnight hours, and it is called as the midnight temperature maximum (MTM) (e.g., Mayr et al., 1979; Herrero and Spencer, 1982; Herrero et al., 1983; Sastri and Rao, 1993; Colerico et al., 1996; Fesen, 1996; Mesquita et al., 2018). Consequently, brightness in redline emission was also enhanced during those events (Colerico and Mendillo, 2002).

The upper atmosphere shows different kinds of variability associated with neutral winds (e.g., Meriwether et al., 1985; Gurubaran et al., 1995; Jyoti et al., 2004; Abdu et al., 2006; Kumar et al., 2022) and electrodynamics (e.g., Pallamraju et al., 1996; Karan et al., 2016; Karan and Pallamraju, 2017; Saha and Pallamraju, 2022). The atmospheric waves have a significant impact on the upper atmosphere at different altitudes (Vadas, 2007; Yiğit and Medevdev, 2009; Miyoshi et al., 2014; Singh and Pallamraju, 2017; Mandal et al., 2020; 2022). Optical and radio techniques have been used to characterize atmospheric waves (e.g., Oliver et al., 1994; Pallamraju et al., 2014, 2016; Mandal et al., 2019; Kumar et al., 2023a). Several model studies have also been carried out, which include the lower atmospheric forcing and describe the thermospheric variation quite satisfactorily (Roble and Ridley, 1994; Fesen, 1996; Laskar et al., 2013; Liu et al., 2018). It is known that atmospheric tides play an essential role in the variation of temperature and winds in the mesosphere and the thermosphere. Several dynamical processes that occur in the upper atmosphere have been explained using the variation in atmospheric tides (e.g., Thayaparan, 1997; Akmaev, 2001; Chau et al., 2009; Guharay and Franke, 2011; Laskar et al., 2014; Guharay et al., 2018; Pedatella and Harvey, 2022; Kumar et al., 2023b). The atmospheric tidal waves are generally generated in the lower atmosphere and they can propagate to the thermosphere where they eventually dissipate due to the molecular viscosity and thermal diffusivity. In the thermosphere, the tides can be generated in-situ as well. The influence of semidiurnal and other higher-order tides was seen during MTM (e.g., Mayr et al., 1979; Herrero et al., 1983; Fesen, 1996; Colerico and Mendillo, 2002), which caused an increase in the nightglow emission intensity during midnight and post-midnight hours. A significant magnitude of MTM was seen in simulations by the Whole Atmosphere Model, and lower atmospheric forcing was found to contribute to the MTM (Akmaev et al., 2009; Fang et al., 2016).

In this work, we have used a free-running version of the Whole Atmosphere Community Climate Model with thermosphere-ionosphere eXtension (WACCM-X) to understand the dynamics prevalent during the post-sunset hours over low-latitudes. Electron densities and meridional winds have been obtained from the WACCM-X at 250 km altitude (which is the altitude of the peak emission of OI 630.0 nm). Interestingly, WACCM-X simulated electron density also occasionally shows an increase after sunset, and the increase is consistent with the presence of poleward winds in the simulation. Therefore, these simulations provide an independent confirmation of the interpretation made in our earlier work that the poleward turning of the usually equatorward meridional wind, or cessation of equatorward wind during post-sunset hours is the cause for the observed enhancements in the OI 630.0 nm emissions from Mt. Abu (Saha et al., 2021). The question we ask in this study is what is the cause for the reversal of meridional wind from its usual equatorward direction at post-sunset hours over low-latitudes?

2. Data used:

2.1. Optical data (OI 630.0 nm nightglow emissions):

An optical spectrograph, High Throughput Imaging Echelle Spectrograph (HiTIES) (Chakrabarti et al., 2001), is used to measure the nocturnal OI 630.0 nm airglow emission variability over a low-latitude location, Mt. Abu. The OI 630.0 nm nightglow emissions originate from an altitude region peaking at around 250 km, with a half-value width of around 70 km. HiTIES is a slit spectrograph, and the spectra around OI 630.0 nm nightglow emissions are imaged onto a 1K×1K CCD chip. Image processing has been carried out to remove the dark counts, scattered lights that arise due to starlight, zodiacal light, and the vignetting and Van-Rhijn effects.

2.2. WACCM-X simulation:

The WACCM-X is a community developed whole atmosphere model that provides simulations of the variabilities in the Earth's atmosphere-ionosphere-thermosphere regions (Liu et al., 2018). The model captures chemical, thermodynamical, electrodynamical, ionization, and physical processes from the surface of the Earth to 500 to 700 km (depending on solar activity) altitudes. The simulation used WACCM4/CAM4 physics, as described in Marsh et al. (2013), Neale et al. (2013), and Liu et al. (2018). The chemistry used in the middle atmosphere chemistry as described in Davis et al. (2023) as well as the ionosphere-thermosphere modifications described in Liu et al. (2018). The model is capable of providing upper atmospheric neutral and ionospheric parameters and dynamics, which are coupled to the lower atmosphere. In this study, the analysis has been carried out using hourly data obtained from a free-run simulation of WACCM-X, where the lower atmospheric dynamics and day-to-day variability are internally generated by the model, for a constant solar flux value of 70 solar flux unit and Ap value of 1 to represent moderate solar activity and geomagnetic quiet conditions, to which the measured data pertains. The global variations in meridional winds, temperatures, and electron densities obtained from WACCM-X are used in this study. The variations in these parameters are analysed to understand the post-sunset emission enhancement observed in the nightglow data. The analyses and results are discussed below.

3. Data analysis and results:

Typically, OI 630.0 nm nightglow emissions show a monotonic decrease after sunset as the ionization stops, but the recombination process of ions and electrons continues uninterruptedly. On several occasions, an enhancement in emissions is observed around 20 to 22 LT following a decrease after sunset (Saha et al., 2021). Figure 1 shows the variations in OI 630.0 nm nightglow enhancements during post-sunset hours for the period of Jan-Mar for the years 2013 to 2016 over Mt. Abu. The thick blue line of Figure 1 shows the typical OI 630.0 nm nightglow variation for a given night in 2016. A total of 72 nights (out of 185 nights) during that period showed an enhancement in post-sunset emissions, as depicted in this figure. Note that all these days were geomagnetically quiet with Ap<20 nT. The left-side y-axis represents the emission rates (in Rayleighs) for the years 2013, 2014, and 2015, whereas, the values shown on the right-side y-axis are for the year 2016. Due to the decrease in the values of solar flux in 2016, the nightglow emission rates are relatively lower as expected, owing to reduced electron number densities. The amount of increase in emissions during post-sunset hours also varies depending on the solar flux (Saha et al., 2021) ranging from a few tens of Rayleigh to around 200 Rayleigh. The occurrence time of nightglow enhancement does not show any dependence on solar flux and seasons.

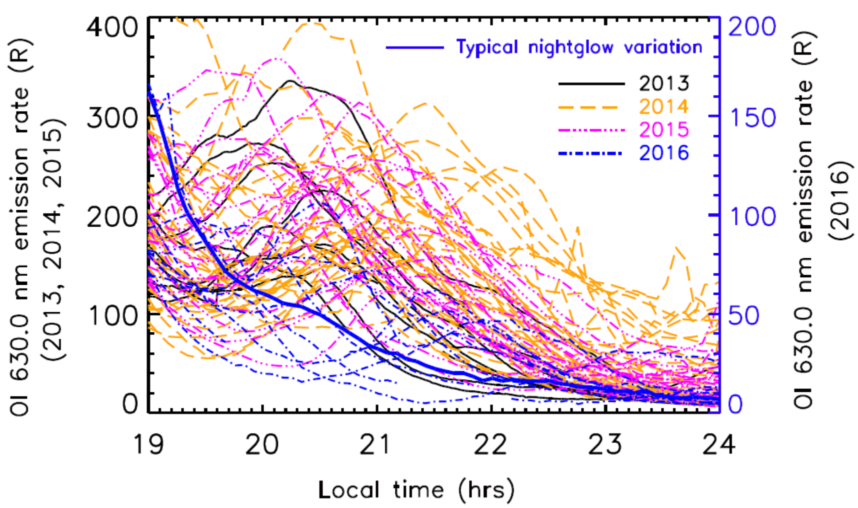

Figure 1: *This is OI 630.0 nm nightglow variations with post-sunset enhancement in emissions for 72 nights from January to March for the years 2013-2016. Typical variation of OI 630.0 nm nightglow emissions has been shown for a given night taken in 2016.*

Figure 2 shows the electron density (top row), meridional wind (middle row), and temperature (bottom row) at 250 km altitude for the location of Mt. Abu as simulated by WACCM-X for three sample days. On these three days, an increase in electron densities is seen after sunset which coincides with the reversal in meridional winds from equatorward to poleward direction. Enhancements in electron densities occur at 21, 23, and 21 LT, respectively, for the three given nights, and the meridional winds show a reversal in the poleward direction at that time. The variation in electron densities at 250 km shows a one-to-one relation with the OI 630.0 nm nightglow emissions for geomagnetic quiet time period, which has been established by the estimated OI 630.0 nm nightglow emissions, wherein the measured electron densities were used as inputs (Saha et al., 2021). Typically, the meridional winds turn equatorward after sunset, but interestingly, a reversal in equatorward wind is seen in the estimated relative variation in meridional winds for a period of 2-3 hours (Saha et al., 2021). The WACCM-X model also shows a similar reversal in meridional winds after sunset, as shown in Figure 2.

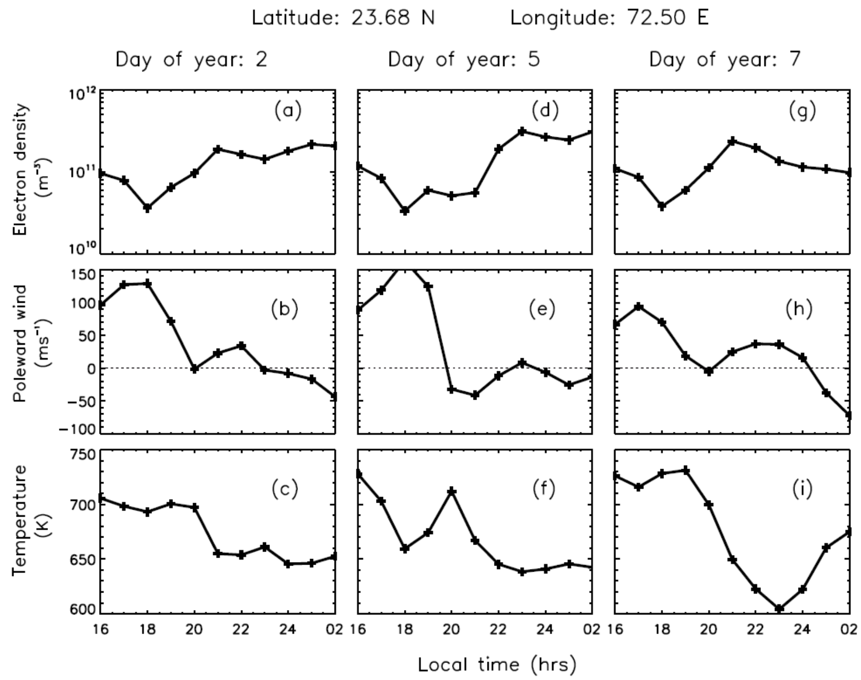

Figure 2: *The electron densities, meridional winds, and temperatures at 250 km altitude are shown for three representative nights obtained from the WACCM-X simulation. An increase in electron densities is seen at 21, 23, and 21 LT, respectively (top panel). Simultaneously, the meridional wind is poleward directed at that time (middle panel). Moreover, the neutral temperature decreases due to the reversal in meridional wind at that time (bottom panel).*

A cumulative picture of the nature of the meridional winds during nighttime is shown in Figure 3 for the months of January, February, and March. During this period, on several occasions, the model shows occurrences of reversal in winds during post-sunset hours. The top panels of Figure 3 show the variation in the meridional winds on those nights when they remain equatorward without any reversal towards poleward direction. In contrast, the bottom panels correspond to those nights when there is a reversal in the meridional winds (or a cessation in their equatorward movement). It can be seen in all the plots that the winds are usually poleward in the daytime and their magnitudes start decreasing during sunset time (typically after 18 LT), and turn equatorward after around 21 LT. It can be noted in the bottom panels that there is a reversal of meridional winds wherein a poleward turn of the meridional winds or weakening of equatorward winds is noted during 21 LT - 01 LT, beyond which it turns again in the equatorward direction. As we move from January to March, the magnitudes of equatorward wind increase during post-sunset hours due to climatological effects, so the number of occurrences of the post-sunset wind reversal decreases. In addition, the model output is derived from a free-run simulation, and it is noteworthy that geophysical events, such as sudden stratospheric warming (SSW), did not occur during the winter analysed in the present study. The simulated variations in the meridional winds are thus not driven by the occurrence of SSW. In the following, we will analyse and discuss the meridional winds obtained from WACCM-X to understand the nature of variation of post-sunset electron density/ redline nightglow emissions for several nights to obtain a systematic picture.

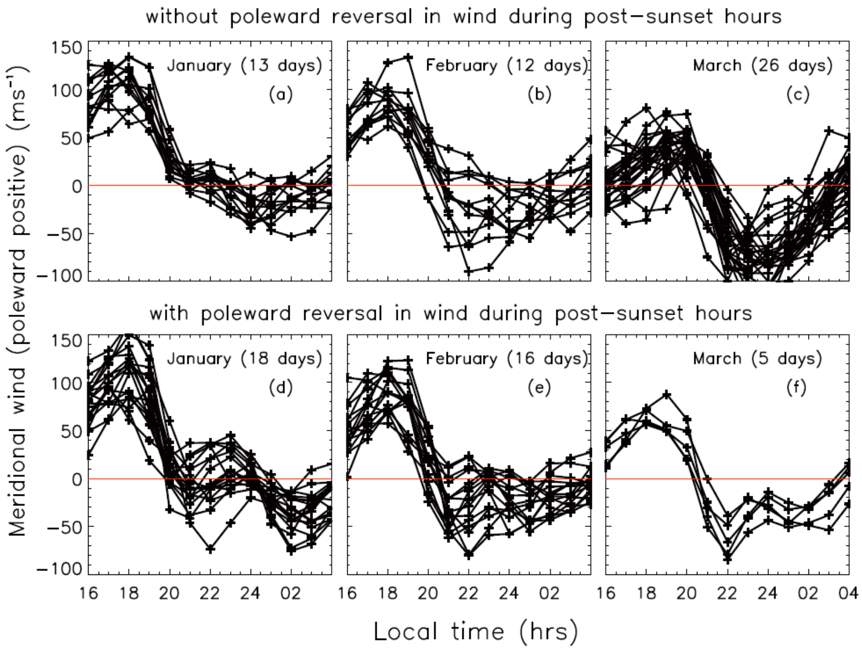

Figure 3: *The nighttime variations in meridional winds obtained from WACCM-X for three different months with two categories, when the meridional wind reversal can be seen during post-sunset hours (bottom panels) and when there is no reversal in meridional winds (top panels).*

Spectral analysis of the WACCM-X meridional winds has been carried out for different days using fast Fourier transform (FFT) for a 24-hour window. Figure 4 shows the meridional winds obtained from the WACCM-X simulation (top panels), and the periodogram analysis (bottom panels) for the three representative nights shown in Figure 2. A residue of 14-hour running average has been considered to investigate the presence of periods smaller than 14 hours. The horizontal red solid lines in the bottom panels indicate a significance level of 80%. The nights used in Figure 4 show a reversal in meridional winds. The significant presence of higher-order tidal periodicities (6h, 8h, and 12h) can be noted on these nights, which motivated further investigations on assessing the contribution of these higher-order tides in the WACCM-X meridional winds.

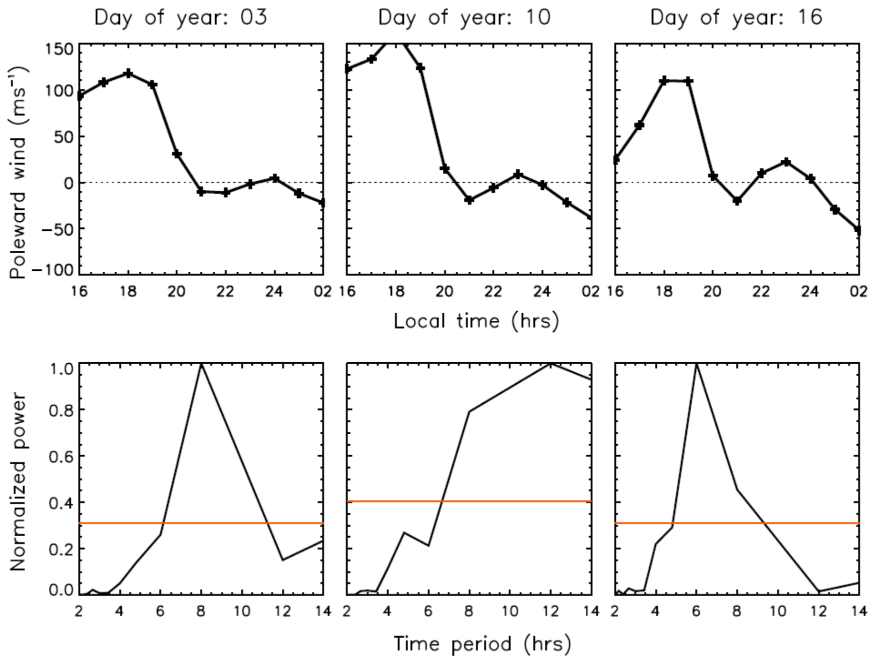

Figure 4: *The meridional wind and power spectral analysis for the three nights shown in Figure 2 in the top and bottom panels, respectively. 80% significance is shown in the FFT power spectrum using red solid lines.*

Based on the above discussion, the hourly meridional winds from WACCM-X are used to estimate the amplitudes of different tidal components for the periodicities at which the FFT analysis showed significant power using the least square fitting method (Venkateswara Rao et al., 2011; Pancheva et al., 2021). We have used the variation of meridional winds simulated by WACCM-X for all the longitudes with a cadence of 2.5° and the latitude has been taken 23.68°, very close to the observation location. Then, the least square fitting has been performed using the following equation:

$$A = A_0 + \sum_{s=-4}^{5} \sum_{i=0}^{3} A_i Sin(\frac{2\pi}{T_i} t + sl + {}_i),\ T_i = 6, 8, 12, 24 \ldots\ldots\ldots.(1)$$

where denotes the mean value, and , , s, and denote the amplitudes, phases of different tidal components, wave numbers, and longitudes, respectively. A window of 24 hours is used in this least square fitting. The amplitudes and phases of these components are obtained from the least square fitting which is further used to derive the temporal behaviour of the winds for a particular tidal component over a given location. The reconstructed winds for all the tidal components are shown in Figure 5 along with the model winds (black solid line) for six representative nights. For each of the nights, different tidal components are identified by different colours, and the sum of these amplitudes and A_0 is shown in the black dash-dot-dot-dot line. A good comparison between the magnitudes of WACCM-X wind and the resultant amplitudes as obtained from equation 1, serves as a validation of the analysis of the least square fit. It can be seen that the diurnal component (magenta dotted line) shows larger magnitude, whereas the amplitudes of other three components, quarter-diurnal (QDT, red long-dashed line), terdiurnal (blue dashed line), and semidiurnal (teal dash-dot line) show comparable magnitudes with each other. The effect of aliasing can arise in the higher-order tidal amplitudes when two tidal components possess the same zonal wave numbers. In our analysis, the model simulation produces continuous data with an hour cadence. Therefore, there is no issue on sampling of the data. Further, we separated the wave numbers of different tidal periodicities using the least square fitting. Therefore, the effect of aliasing will not reflect in the obtained amplitudes of different tides. As the migrating component of diurnal and semi-diurnal tides have larger magnitude, they can be aliased into higher-order tides with same wave numbers with greater magnitudes (Moudden and Forbes, 2013). However, the amplitudes of wave numbers 1 and 2 in QDTs and terdiurnal tides appear very small. We have also used a 7h filter to remove the contribution of higher-order tides which we have also discussed in later. The amplitudes of QDTs obtained after 7h filtering remain the same as calculated from equation 1. The result further verifies that the obtained amplitudes do not contain the effect of aliasing in the higher-order tides.

Broadly, the winds are poleward and equatorward in the daytime and nighttime, respectively, as seen in the strong diurnal component. The amplitudes and phases of different tidal components contribute differently to the resultant variations of meridional winds. The subtle variations in the winds can be due to the influence of higher-order tidal contributions. For example, the winds are poleward in the daytime, but due to the opposite phase of other tidal components, a double-humped structure can be seen in the model wind during daytime. After sunset, the winds turn equatorward. On occasions, the meridional winds reverse their direction from equatorward to poleward after sunset (Figure 5). The shaded regions of Figure 5 indicate the duration when the reversal in meridional winds can be seen. On such occasions, we can see that the magnitudes of the QDT vary concurrently with the winds thereby, it is likely responsible for causing the reversal in the meridional winds. The magnitude of the winds after post-sunset reversal gets even stronger when the phases of the other three tidal components match one another. For example, on the day of year 7 (Figure 5d), we see a larger increase in the magnitude of winds during post-sunset time, and interestingly, quarter-diurnal, terdiurnal, and semidiurnal tides seem to be occurring in phase. Figure 6 shows the reconstructed winds while QDT has not been considered in the reconstruction. A clear difference can be seen, especially in the wind variation during post-sunset hours. When the QDT is absent, the reversal in winds is not being generated and the winds show the usual variation of poleward to equatorward.

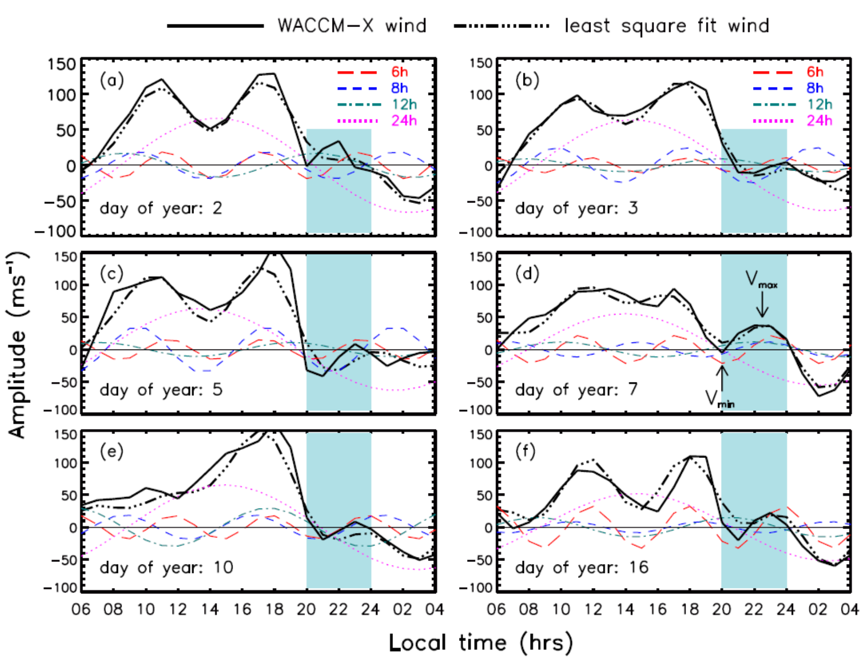

Figure 5: *Four tidal components obtained by the least square fitting in the WACCM-X simulated meridional wind output for 6 sample days. The shaded regions indicate the post-sunset hours when the reversal in meridional winds can be seen. The changes in wind magnitudes are calculated from minimum (V_{min}) and maximum (V_{max}) wind values during such reversals.*

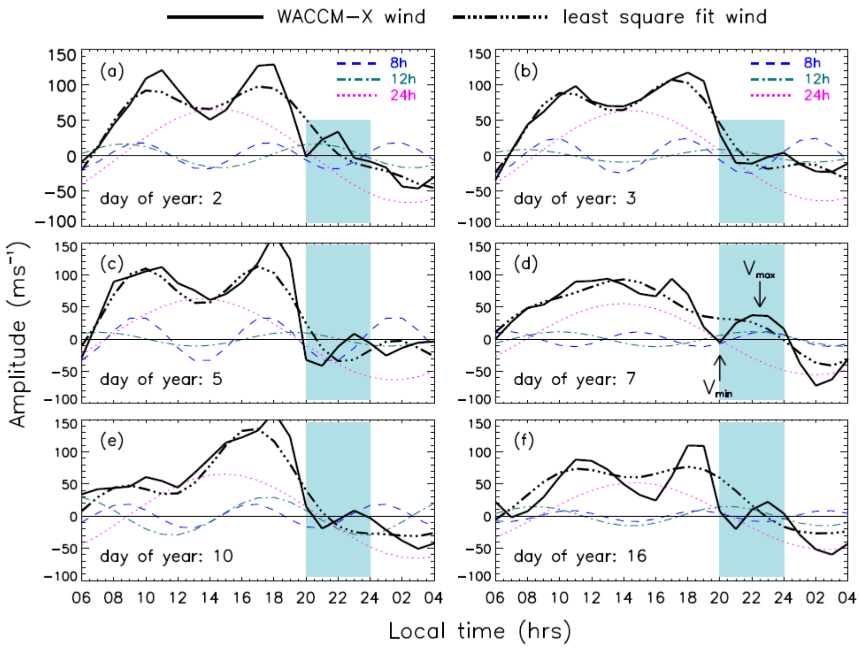

Figure 6: *Only difference with Figure 5 is that QDT has not been taken while reconstructing the winds. The post-sunset winds do not show reversal clearly without the inclusion of QDT.*

We have also verified the amplitude of higher-order tides by analysing the WACCM-X simulated winds using a 7h band-pass filter (Moudden and Forbes, 2013; Gong et al., 2023). The least square fitting method was applied after processing the winds of a given location by a 7h band-pass filter. The 7h band-pass filter diminishes the contribution arising from semi-diurnal and diurnal tides, which predominantly contribute to the meridional wind variation. The effect of aliasing, if any, due to these tides will also be reduced using this technique (Moudden and Forbes, 2013). The amplitude of QDTs obtained using this calculation aligns with the result obtained by the earlier-mentioned method, wherein the wave number and the corresponding tidal periodicities were used. This demonstrates that the higher-order tides do not contain the aliasing effect in the analysis as carried out in this study.

4. Discussion:

In the previous section, we have discussed the post-sunset enhancement in electron density as obtained from WACCM-X over low-latitudes which agrees well with enhancements in the OI 630.0 nm nightglow emissions after sunset (Figure 1). The spectral analysis and least square fit indicate the contribution of tidal components in the meridional wind variation obtained from WACCM-X. The least square fit provides the amplitude and phase information of different tidal components such as diurnal, semi-diurnal, terdiurnal, and quarter-diurnal, which depicts a picture that helps in understanding the tidal contribution to the meridional wind variation. The top panel (panel a) of Figure 7 shows the amplitude variation of four tidal components during the period from January to March. The amplitudes of diurnal tides can be seen to be larger as compared to the other three components, which show reasonably similar amplitudes, as also mentioned above for a few days. The quarter-diurnal tides have been shown to be responsible for the reversal of post-sunset hour meridional winds, as demonstrated for a few days, as shown in Figure 5. The variations in phase and amplitude of the higher-order tides, such as terdiurnal and quarter-diurnal are depicted in the panels b and c of Figure 7, respectively. The phases of QDTs coincide with the time of wind reversal, and the amplitudes of QDTs are also larger when the model shows an increase in the electron density. This is in simultaneity with the time when a maximum in poleward wind magnitudes occurs in the post-sunset hours. The bottom panel (panel d) of Figure 7 shows the changes in wind magnitudes from those at the time of the abatement of equatorward wind (V_{min}, as shown in Figure 5d) and its peak value after that reversal (V_{max}, as shown in Figure 5d). Depending on the amplitude and phase of QDT, the change in wind magnitude shows day-to-day variations (Figure 7). For example, the reduction/absence in wind reversal can be seen, as shaded with light blue colour, with the simultaneous reduction in amplitude of QDT. Besides, an increase in the amplitude of QDT and significant changes in wind magnitudes are seen, as shaded in salmon colour. Reference lines are drawn in Figure 7 (panels c and d) for the amplitude of QDT and magnitude of wind reversal at the values 16 and 25 $\mathrm{ms^{-1}}$, respectively. It can be seen that whenever the magnitudes of wind reversal exceed 25 $\mathrm{ms^{-1}}$, the amplitudes of QDTs are greater than 16 $\mathrm{ms^{-1}}$, and the times of peak phase values are seen to be around or before midnight. As discussed earlier, the time of the phases of different tides is also important. When the peaks in the phases of different periodicities, such as QDTs, terdiunal, and semidiurnal tides align in time, there can be further amplification in the wind magnitudes. For instance, we have seen a larger magnitude in wind reversal on DOY 7 due to the synchronization of phases of these three tidal components (Figure 5d). Such phase matching of these three tidal components is also seen for days 14 and 17. As the phases of QDTs are seen to be shifted beyond midnight towards the end of March, no reversal in winds in the post-sunset hours is observed. In this way, the amplitudes and phases of different tidal components, such as quarter-diurnal, terdiurnal, and semidiurnal tides, come out as important factors for the occurrence of reversal in the post-sunset wind, with the QDTs as the major contributor.

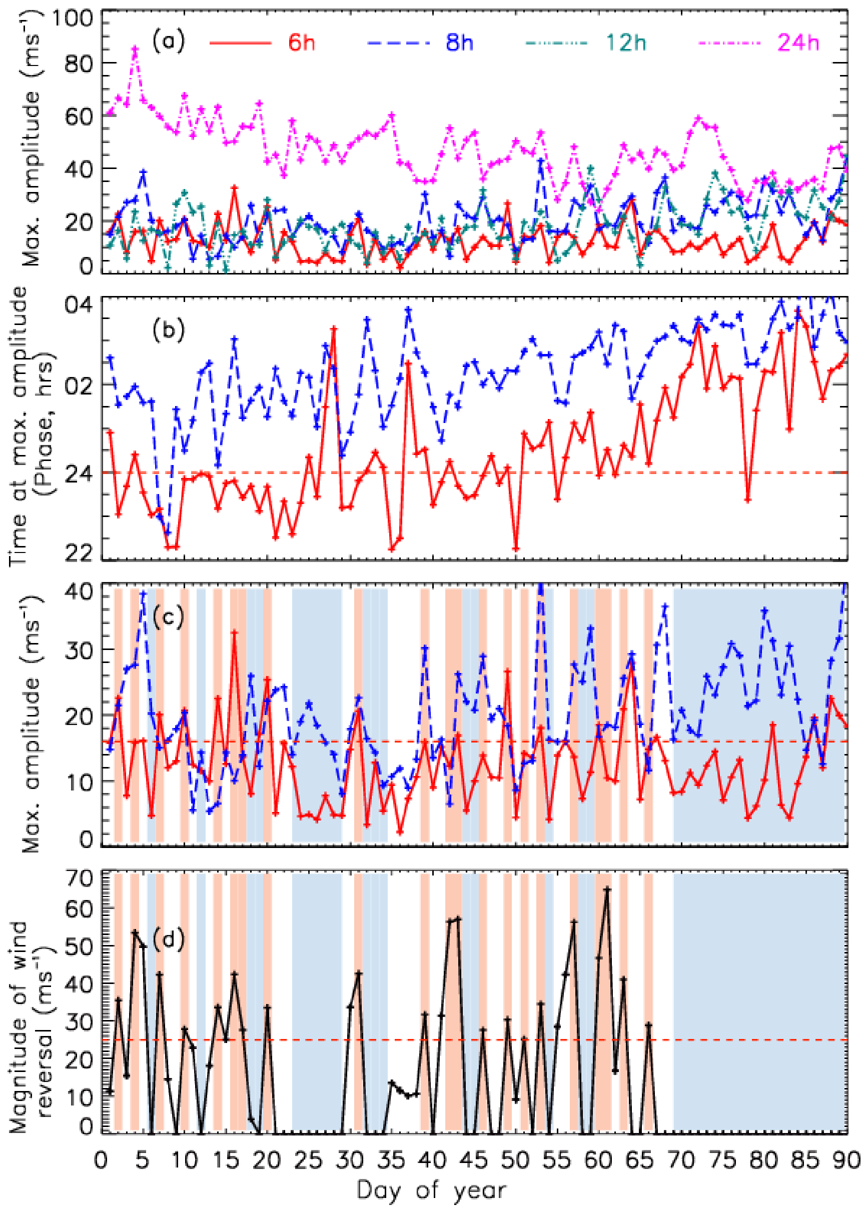

Figure 7: *The amplitudes of different tides are shown in panel (a) for different days from January to March as obtained from the WACCM-X simulated meridional winds. Panels (b) and (c) show the phases and amplitudes of the quarter-diurnal and terdiurnal tidal components for the same duration, respectively. The bottom panel (d) depicts the change in wind magnitude after the post-sunset reversal in the wind. The shaded regions with salmon colour indicate the presence of wind reversal, and the magnitude of wind reversal can be seen to correspond with the amplitude of QDT. The blue shaded regions indicate the days when reversals were not seen, and the amplitudes of QDT were small. Reference lines have been marked for magnitude of wind reversal and maximum amplitude of QDT at the values of 25 and 16 ms^{-1}, respectively. The phase of QDT, a reference line marked at 24 LT, also plays an important role. Whenever the magnitudes of wind reversal are greater than 25 ms^{-1}, on most occasions, the amplitudes of QDT are greater than 16 ms^{-1} and phases are present at pre-midnight time.*

We have investigated the post-sunset enhancement in electron density, which follows the reversal in meridional winds after sunset for January to March as obtained from WACCM-X simulations. Out of a total of 90 days from January to March, we have found such reversal in winds on 39 days during post-sunset times in the WACCM-X simulation. The amplitude of different tidal components, as well as the superposition of those components, were calculated and compared with the change in wind magnitudes after the reversal. As can be seen, the broad meridional wind pattern follows the diurnal tidal component. Therefore, we removed the contribution of the large background diurnal component. The changes in wind magnitudes have been calculated considering the contribution of quarter-diurnal, terdiurnal, and semi-diurnal components only, which are shown to be responsible for the reversal in wind. The changes in amplitude of different tidal components have been calculated between the time of V_{min} and V_{max} (as shown in Figure 5d). Figure 8 shows the relation between the changes in amplitude of the (a) quarter-diurnal, (b) terdiurnal, and (c) semidiurnal tides with the changes in wind magnitudes wherein the diurnal contribution has been subtracted. The amplitudes of QDT show a clear positive relation with the change in wind magnitude, whereas the other tidal components contribute at small magnitudes. Collectively, when the phases of these tides match, they also give rise to larger changes in the wind magnitudes. Therefore, based on the detailed analysis and results as depicted in Figures 5, 6, 7, and 8a, it can be concluded that the magnitudes of quarter-diurnal tide play a major role in the reversal of meridional winds as seen during post-sunset hours.

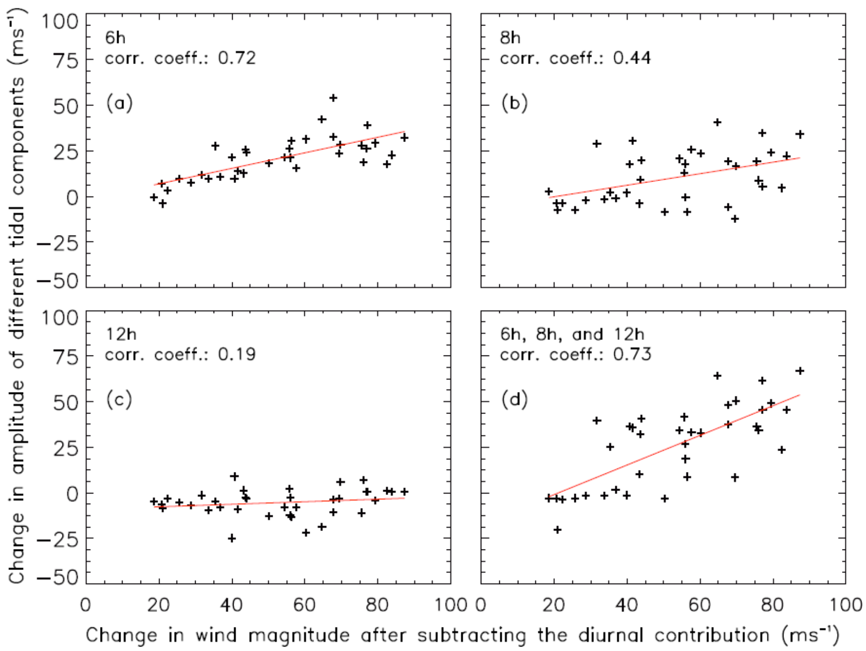

Figure 8: *The x-axis depicts the change in wind magnitude during the post-sunset wind reversal obtained by subtracting the contribution of diurnal tide amplitudes. The change in tidal components during the wind reversal period is depicted on the y-axis. Different panels show variations in the changes in amplitudes of different tides with the change in wind magnitudes. The quarter-diurnal tide shows the best correlation with the wind reversal.*

The diurnal variation in tides is clearly seen in the broad picture of meridional wind variation. Typically, winds are poleward and equatorward during the day and nighttime, respectively (Figure 5). The small-scale variations are seen due to other tidal components, such as, semi-diurnal, terdiurnal, and quarter-diurnal. Higher-order tides, such as terdiurnal and quarter-diurnal, have been investigated at lower thermosphere altitudes using the temperature and wind data obtained from both measurements and models (Moudden and Forbes, 2013; Guharay et al., 2018; Jacobi et al., 2017; Pancheva et al., 2021). In a recent work, the climatological mean amplitude of QDTs has been shown to be comparable with semi-diurnal and terdiurnal in the thermospheric altitude of around 250 km as measured by incoherent scatter radar over Arecibo (Gong et al., 2023). The quarter-diurnal and terdiurnal tides in the upper atmospheric altitudes can be generated in different ways. Both the migrating and non-migrating tides can play a significant role here. However, thermal excitation by the solar heating and non-linear wave-wave interaction can generate the higher-order tides of different wavenumbers in the middle and upper atmosphere (Xu et al., 2012, 2014; Moudden and Forbes, 2013; Geißler et al., 2020). Although the amplitude of these higher-order tides is significantly small compared to diurnal tides, they nonetheless seem to play an important role in the dynamics of the thermosphere, especially in the post-sunset hours. Here, we show that the QDTs are more effective in causing the reversal in meridional winds after sunset, which has not been reported so far, to the best of our knowledge.

5. Summary:

The OI 630.0 nm nightglow emission brightness typically shows a monotonic decrease after sunset. On many occasions, an enhancement in emissions has been observed during post-sunset hours as measured by HiTIES over Mt. Abu, a low-latitude location in India. In a comprehensive and detailed investigation, the presence of poleward wind has been shown to be responsible for such enhancement in emissions at low latitudes as the poleward winds bring down the plasma to lower altitudes (Saha et al., 2021). The cause of such reversal in the usually equatorward winds at post-sunset hours has been examined in this study. In order to address the optical observations, free-running WACCM-X simulations have been carried out for a three-month duration, which also showed an increase in electron density during post-sunset hours on many occasions in the altitudinal region of 250 km, as also shown in the digisonde measurements in our earlier study (Saha et al., 2021). The WACCM-X simulations show a reversal of equatorward wind coincident with the time of enhancement in electron density, which serves as an independent confirmation of our observations reported earlier (Saha et al., 2021). In the present work, the variations of meridional winds obtained from WACCM-X have been analysed to understand the cause of such reversals during the post-sunset time. Different tidal periodicities, such as diurnal, semidiurnal, terdiurnal, and quarter-diurnal, are fitted using least square method, which reveals very interesting information on the amplitudes and phases of each of the components and their association with the direction of the meridional wind. The phase and amplitude of higher-order tides play a crucial role in the nighttime thermospheric dynamics. Whenever the amplitudes of higher-order tides fall in the same phase, the magnitudes of wind reversal get enhanced. Thereby, a strong tidal contribution has been found to be the cause behind the poleward reversal of meridional winds after sunset, which causes an increase in electron density as well as enhancement in OI 630.0 nm emission. Especially, QDTs play the dominant role in the variation of meridional wind. This also explains why such reversals in winds do not occur on all the nights in a given season. Thus, the redline OI 630.0 nm emission enhancements in the post-sunset time can also serve as an indicator of the reversal of winds and the existence of the strength of the higher-order tides at that time.

6. Acknowledgement:

The nighttime optical data, used in this study, has been obtained by the Physical Research Laboratory, Ahmedabad, India. This work is supported by the Department of Space, Government of India. FL was supported by NASA Contract 80GSFC18C0061 to the University of Colorado, Boulder, USA.

7. Open Research:

The data used to represent the figures in this work can be accessed from https://osf.io/gteq9/. A netCDF file containing all the relevant WACCM-X simulated data used in this study is available at the following link: https://doi.org/10.5281/zenodo.8400600.

8. References:

Abdu, M. A., Iyer, K. N., de Medeiros, R. T., Batista, I. S., & Sobral, J. H. (2006). Thermospheric meridional wind control of equatorial spread F and evening prereversal electric field. *Geophysical research letters*, *33*(7). https://doi.org/10.1029/2005GL024835.

Akmaev, R.A. (2001). Seasonal variations of the terdiurnal tide in the mesosphere and lower thermosphere: A model study. Geophysical Research Letter, 28, 3817-3820. https://doi.org/10.1029/2001GL013002.

Akmaev, R. A., Wu, F., Fuller-Rowell, T. J., & Wang, H. (2009). Midnight temperature maximum (MTM) in Whole Atmosphere Model (WAM) simulations. Geophysical Research Letter, 36, L07108, https://doi.org/10.1029/2009GL037759.

Chakrabarti, S., Pallamraju, D., Baumgardner, J., & Vaillancourt, J. (2001). HiTIES: A High Throughput Imaging Echelle Spectrograph for ground-based visible airglow and auroral studies. Journal of Geophysical Research, 106(A12), 30,337-30,34. https://doi.org/10.1029/2001JA001105.

Chau JL, Fejer BG, & Goncharenko LP (2009). Quiet variability of equatorial E x B drifts during a sudden stratospheric warming event. Geophysical Research Letter, 36, L05101. https://doi.org/10.1029/2008GL036785.

Colerico, M., Mendillo, M., Nottingham, D., Baumgardner, J., Meriwether, J., Mirick, J., . . . & Biondi, M. A. (1996). Coordinated measurements of F region dynamics related to the thermospheric midnight temperature maximum. Journal of Geophysical Research: Space Physics, 101(A12), 26783-26793. https://doi.org/10.1029/96JA02337.

Colerico, M. J., & Mendillo, M. (2002). The current state of investigations regarding the thermospheric midnight temperature maximum (MTM). Journal of atmospheric and solar-terrestrial physics, 64(12-14), 1361-1369. https://doi.org/10.1016/S1364-6826(02)00099-8.

Davis, N. A., Visioni, D., Garcia, R. R., Kinnison, D. E., Marsh, D. R., Mills, M., et al. (2023). Climate, variability, and climate sensitivity of “Middle Atmosphere” chemistry configurations of the Community Earth System Model Version 2, Whole Atmosphere Community Climate Model Version 6 (CESM2(WACCM6)). *Journal of Advances in Modeling Earth Systems*, 15, e2022MS003579. https://doi.org/10.1029/2022MS003579.

Fang, T. W., Akmaev, R. A., Stoneback, R. A., Fuller-Rowell, T., Wang, H., & Wu, F. (2016). Impact of midnight thermosphere dynamics on the equatorial ionospheric vertical drifts. *Journal of Geophysical Research: Space Physics*, *121*(5), 4858-4868. https://doi.org/10.1002/2015JA022282.

Fesen, C. G. (1996). Simulations of the low-latitude midnight temperature maximum. Journal of Geophysical Research: Space Physics, 101(A12), 26863-26874. https://doi.org/10.1029/96JA01823.

Geissler, C., Jacobi, C., and Lilienthal, F. (2020). Forcing mechanisms of the migrating quarterdiurnal tide, Annales Geophysicae, 38, 527–544. https://doi.org/10.5194/angeo-38-527-2020.

Gong Y, Ding Y, Chen X, Zhang S, Zhou Q, Ma Z, & Luo J. (2023). Long-Term Observations of the Thermospheric 6 h Oscillation Revealed by an Incoherent Scatter Radar over Arecibo. *Remote Sensing*, 15(21), 5098. https://doi.org/10.3390/rs15215098.

Guharay A. & Franke S. J. (2011). Characteristics of the semidiurnal tide in the MLT over Maui (20.75degN, 156.43degW) with meteor radar observations. Journal of atmospheric and solar-terrestrial physics, 73, 678–685. https://doi.org/10.1016/j.jastp.2011.01.025.

Guharay, A., Batista, P. P., Buriti, R. A., & Schuch, N. J. (2018). On the variability of the quarter-diurnal tide in the MLT over Brazilian low-latitude stations. Earth, Planets and Space, 70, 1-14. https://doi.org/10.1186/s40623-018-0910-9.

Gurubaran, S., Sridharan, R., & Raghavarao, R. (1995). Effects of neutral temperature on meridional winds estimated from ionospheric data. *Journal of Atmospheric and Terrestrial Physics*, *57*(10), 1095-1101. https://doi.org/10.1016/0021-9169(94)00125-8.

Herrero, F. A., & Spencer, N. W. (1982). On the horizontal distribution of the equatorial thermospheric midnight temperature maximum and its seasonal variation. Geophysical Research Letters, 9(10), 1179-1182. https://doi.org/10.1029/GL009i010p01179.

Herrero, F. A., Mayr, H. G., & Spencer, N. W. (1983). Latitudinal (seasonal) variations in the thermospheric midnight temperature maximum: A tidal analysis. Journal of Geophysical Research: Space Physics, 88(A9), 7225-7235. https://doi.org/10.1029/JA088iA09p07225.

Jacobi, C., Krug A., Merzlyakov, E. (2017). Radar observations of the quarterdiurnal tide at midlatitudes: Seasonal and long-term variations, Journal of Atmospheric and Solar-Terrestrial Physics, 163, 70-77. https://doi.org/10.1016/j.jastp.2017.05.014.

Jyoti, N., Devasia, C. V., Sridharan, R., & Tiwari, D. (2004). Threshold height $(h'F)_c$ for the meridional wind to play a deterministic role in the bottom side equatorial spread F and its dependence on solar activity, *Geophysical Research Letter*, 31, L12809. https://doi.org/10.1029/2004GL019455.

Karan, D. K., Pallamraju, D., Phadke, K. A., Vijayalakshmi, T., Pant, T. K., & Mukherjee, S. (2016). Electrodynamic influence on the diurnal behavior of neutral daytime airglow emissions. Annales Geophysicae, 34, 1019–1030. https://doi.org/10.5194/angeo-34-1019-2016.

Karan, D. K., & Pallamraju, D. (2017). Small-scale longitudinal variations in the daytime equatorial thermospheric wave dynamics as inferred from oxygen dayglow emissions. Journal of Geophysical Research, Space Physics, 122, 6528–6542. https://doi.org/10.1002/2017JA023891.

Kumar, S., Pallamraju, D., Suryawanshi, P., Vijayalakshmi, T., & Seemala, G. K. (2022). On the latitudinal variation in oi 630.0 nm dayglow emissions in response to the equatorial electrodynamic processes and neutral winds. Advances in Space Research, 69(2), 926–938. https://doi.org/10.1016/j.asr.2021.10.034.

Kumar, S., Mandal, S., & Pallamraju, D. (2023a). Characterization of gravity waves in three dimensions in the daytime thermosphere using combined optical and radio measurements and estimation of horizontal neutral winds. Journal of Geophysical Research: Space Physics, 128(3), e2022JA030954. https://doi.org/10.1029/2022JA030954.

Kumar, S., Siddiqui, T.A., Stolle, C., Pedatella, N. M., & Pallamraju, D. (2023b). Impact of strong and weak stratospheric polar vortices on geomagnetic semidiurnal solar and lunar tides. Earth Planets Space **75**, 52. https://doi.org/10.1186/s40623-023-01810-x.

Laskar, F. I., Pallamraju, D., Lakshmi, T. V., Reddy, M. A., Pathan, B.M., & Chakrabarti, S. (2013). Investigations on vertical coupling of atmospheric regions using combined multiwavelength optical dayglow, magnetic, and radio measurements. Journal of Geophysical Research, Space Physics, 118 (7), 4618–4627. http://dx.doi.org/10.1002/jgra.50426.

Laskar, F.I., Pallamraju, D., & Veenadhari, B. (2014). Vertical coupling of atmospheres: dependence on strength of sudden stratospheric warming and solar activity. Earth Planets Space 66 (1), 94. http://dx.doi.org/10.1186/1880-5981-66-94.

Liu, H.-L., Bardeen, C. G., Foster, B. T., Lauritzen, P., Liu, J., Lu, G., . . . Wang, W. (2018). Development and validation of the Whole Atmosphere Community Climate Model with thermosphere and ionosphere extension (WACCM-X 2.0). Journal of Advances in Modeling Earth Systems, 10, 381– 402. https://doi.org/10.1002/2017MS001232.

Mandal, S., Pallamraju, D., Karan, D., Phadke, K., Singh, R., & Suryawanshi, P. (2019). On deriving gravity wave characteristics in the daytime upper atmosphere using radio technique. Journal of Geophysical Research: Space Physics, 124(8), 6985–6997. https://doi.org/10.1029/2019JA026723.

Mandal, S., & Pallamraju, D. (2020). Thermospheric gravity wave characteristics in the daytime over low-latitudes during geomagnetic quiet and disturbed conditions. Journal of Atmospheric and Solar-Terrestrial Physics, 211, 105470. https://doi.org/10.1016/j.jastp.2020.105470.

Mandal, S., Pallamraju, D., & Pant, T. (2022). Vertical propagation speeds of gravity waves in the daytime as a precursor to the onset of the equatorial spread-f. Journal of Geophysical Research: Space Physics, 127(8). https://doi.org/10.1029/2022JA030401.

Marsh, D. R., Mills, M. J., Kinnison, D. E., Lamarque, J., Calvo, N., & Polvani, L. M. (2013). Climate Change from 1850 to 2005 Simulated in CESM1(WACCM). *Journal of Climate, 26(19), 7372-7391.* https://doi.org/10.1175/JCLI-D-12-00558.1

Mayr, H.G., Harris, I., Spencer, N.W., Hedin, A.E., Wharton, L.E., Potter, H.S., Walker, J.C.G., & Carlson, H.C. (1979). Tides and the midnight temperature anomaly in the thermosphere. Geophysical Research Letters 6, 447–450. https://doi.org/10.1029/GL006i006p00447.

Meriwether, J. W., Jr., Biondi, M. A., & Anderson, D. N. (1985). Equatorial airglow depletions induced by thermospheric winds. Geophysical Research Letters, 12, 487. https://doi.org/10.1029/GL012i008p00487.

Mesquita, R. L., Meriwether, J. W., Makela, J. J., Fisher, D. J., Harding, B. J., Sanders, S. C., . . . & Ridley, A. J. (2018). New results on the mid-latitude midnight temperature maximum. In Annales Geophysicae, 36, 2, 541-553. Gottingen, Germany: Copernicus Publications. https://doi.org/10.5194/angeo-36-541-2018.

Miyoshi, Y., Fujiwara, H., Jin, H., & Shinagawa, H. (2014). A global view of gravity waves in the thermosphere simulated by a general circulation model. *Journal of Geophysical Research: Space Physics*, *119*(7), 5807–5820. https://doi.org/10.1002/2014JA019848.

Moudden, Y., and Forbes, J. M. (2014), Quasi-two-day wave structure, interannual variability, and tidal interactions during the 2002–2011 decade, *Journal of Geophysical Research: Atmospheres*, 119, 2241–2260, doi:10.1002/2013JD020563.

Neale, R. B., Richter, J., Park, S., Lauritzen, P. H., Vavrus, S. J., Rasch, P. J., & Zhang, M. (2013). The Mean Climate of the Community Atmosphere Model (CAM4) in Forced SST and Fully Coupled Experiments. *Journal of Climate*, *26*(14), 5150-5168. https://doi.org/10.1175/JCLI-D-12-00236.1

Oliver, W. L., Fukao, S., Yamamoto, Y., Takami, T., Yamanaka, M. D., Yamamoto, M., et al. (1994). Middle and upper atmosphere radar observations of ionospheric density gradients produced by gravity wave packets. Journal of Geophysical Research, 99(A4), 6321–6329. https://doi.org/10.1029/94JA00171.

Pallam Raju, D., Sridharan, R., Gurubaran, S., & Raghavarao, R. (1996). First results from ground-based daytime optical investigation of the development of the equatorial ionization anomaly. Annales Geophysicae, 14(2), 238–245. https://doi.org/10.1007/s00585-996-0238-9.

Pallamraju, D., Baumgardner, J., Singh, R. P., Laskar, F. I., Mendillo, C., Cook, T., et al. (2014). Daytime wave characteristics in the mesosphere lower thermosphere region: Results from the Balloon-borne Investigations of Regional-atmospheric Dynamics experiment, Journal of Geophysical Research, 119, 2229-2242. https://doi.org/10.1002/2013JA019368.

Pallamraju, D., Karan, D. K., & Phadke, K. A. (2016). First three-dimensional wave characteristics in the daytime upper atmosphere derived from ground-based multiwavelength oxygen dayglow emission measurements, Geophysical Research Letters, 43, 5545–5553. https://doi.org/10.1002/2016GL069074.

Pancheva, D., Mukhtarov, P., Hall, C., Smith, A.K., & Tsutsumi, M. (2021). Climatology of the short-period (8-h and 6-h) tides observed by meteor radars at Tromso and Svalbard, Journal of Atmospheric and Solar-Terrestrial Physics, 212, 105513. https://doi.org/10.1016/j.jastp.2020.105513.

Pedatella NM, & Harvey VL. (2022) Impact of strong and weak stratospheric polar vortices on the mesosphere and lower thermosphere. Geophysical Research Letter 49, e2022GL098877. https:// doi. org/ 10. 1029/ 2022G L0988 77.

Roble, R. G., & Ridley, E. C. (1994). A thermosphere-ionosphere-mesosphere-electrodynamics general circulation model (TIME-GCM): Equinox solar cycle minimum simulations (30–500 km). *Geophysical Research Letters*, *21*(6), 417-420. https://doi.org/10.1029/93GL03391.

Saha, S., Pallamraju, D., Pant, T. K., & Chakrabarti, S. (2021). On the cause of the post-sunset nocturnal OI 630 nm airglow enhancement over low-latitude thermosphere. Journal of Geophysical Research: Space Physics, 126, e2021JA029146. https://doi.org/10.1029/2021JA029146.

Saha, S. & Pallamraju, D. (2022). Latitudinal Variations in the Nocturnal behaviour of OI 630 nm Airglow Emissions and their relationship with the Equatorial Electrodynamics. Journal of Atmospheric and Solar-Terrestrial Physics, 241, 105965. https://doi.org/10.1016/j.jastp.2022.105965.

Sastri, J. H., & Rao, H. R. (1994). Optical interferometer measurements of thermospheric temperature at Kavalur (12.5 N, 78.5 E), India. Journal of atmospheric and terrestrial physics, 56(6), 775-782. https://doi.org/10.1016/0021-9169(94)90132-5

Singh, R. P., & Pallamraju, D. (2017). Large- and small-scale periodicities in the mesosphere as obtained from variations in O_2 and OH nightglow emissions, Annales Geophysicae, 35, 227–237, https://doi.org/10.5194/angeo-35-227-2017.

Thayaparan, T. (1997). The terdiurnal tide in the mesosphere and lower thermosphere over London, Canada (43degN, 81degW). *Journal of Geophysical Research*, 102 (D18), 21695– 21708. https://doi.org/10.1029/97JD01839.

Vadas, S. L. (2007). Horizontal and vertical propagation and dissipation of gravity waves in the thermosphere from lower atmospheric and thermospheric sources. Journal of Geophysical Research Space Physics, 112(A6). https://doi.org/10.1029/2006JA011845.

Venkateswara Rao, N., Tsuda, T., Gurubaran, S., Miyoshi, Y., and Fujiwara, H. (2011). On the occurrence and variability of the terdiurnal tide in the equatorial mesosphere and lower thermosphere and a comparison with the Kyushu-GCM, *Journal of Geophysical Research: Atmospheres*, 116, D02117. https://doi.org/10.1029/2010JD014529.

Xu, J., Smith, A. K., Jiang, G., Yuan, W., and Gao, H. (2012). Features of the seasonal variation of the semidiurnal, terdiurnal and 6-h components of ozone heating evaluated from Aura/MLS observations, *Annales Geophysicae*, 30, 259–281, https://doi.org/10.5194/angeo-30-259-2012.

Xu, J., Smith, A. K., Liu, M., Liu, X., Gao, H., Jiang, G., and Yuan, W. (2014), Evidence for nonmigrating tides produced by the interaction between tides and stationary planetary waves in the stratosphere and lower mesosphere, *Journal of Geophysical Research Atmosphere*, 119, 471–489, doi:10.1002/2013JD020150.

Yiğit, E., & Medvedev, A. S. (2009). Heating and cooling of the thermosphere by internal gravity waves. *Geophysical Research Letters*, *36*(14), L14807. https://doi.org/10.1029/2009GL038507.